

Spin-canting effects in GMR sensors with wide dynamic field range

Clemens Muehlenhoff,^{1,2,*} Christoph Vogler,^{3,†} Wolfgang Raberg,² Dieter Suess,³ and Manfred Albrecht¹

¹*Institute of Physics, University of Augsburg, Augsburg 86159, Germany*

²*Infineon Technologies AG, 85579 Neubiberg, Germany*

³*Christian Doppler Laboratory for Advanced Magnetic Sensing and Materials, Faculty of Physics, University of Vienna, Boltzmannngasse 5, 1090 Vienna, Austria*

Magnetoresistive (xMR) sensors find extensive application in science and industry, replacing Hall sensors in various low field environments. While there have been some efforts in increasing the dynamic field range of xMR sensors, Hall sensors remain to dominate high field applications due to their wide linear range. Using a perpendicular magnetized reference system and an in-plane free layer allows us to overcome this disadvantage of xMR sensors, and, furthermore, investigate spin-canting effects in interlayer exchange coupled perpendicular synthetic antiferromagnets (p-SAF). We created p-SAFs with exchange coupling fields of up to 10 kOe, based on magnetic Co/Pt multilayer systems. The p-SAFs are either designed as "single" p-SAFs, where two Co/Pt multilayers are interlayer exchange coupled via a 4 Å thick Ru spacer, or as "double" p-SAFs, where an additional Co layer is interlayer exchange coupled to the top multilayer. These p-SAFs are used for giant magnetoresistance (GMR) sensors with wide dynamic field range. By using a p-SAF as the reference system and employing an in-plane magnetic layer as the GMR's free layer, the linear range can be effectively increased limited only by the p-SAF's switching fields. Additionally, the magnetic anisotropy of the in-plane free layer is fully controlled, which allows saturation fields by design. With this, the entire spectrum from parallel to antiparallel alignment of free and reference layer is exploited, which yields the full GMR signal potential. Different configurations were investigated, ranging from free layer magnetic saturation at lower to far higher fields than the p-SAF's switching fields. We can show through micromagnetic simulations that certain GMR transfer curves are dominated by spin-canting effects in the interlayer exchange coupled reference system. Finally, our simulation results lay out the correlation of the p-SAF's design parameters and its magnetization reversal behavior.

I. INTRODUCTION

Magnetoresistive (xMR) effects, such as the giant (GMR) [1] or the tunneling magnetoresistance (TMR) [2], are already established devices for modern day technologies [3–6]. Besides their application in Hard Disk Drive (HDD) read heads, xMR sensors have also replaced Hall sensors in many areas, due to their superior sensitivity, high frequency bandwidth, and low power consumption [7, 8]. However, there are still properties of the Hall sensor, in which xMR based sensors cannot compete. These properties include an out-of-plane sensitivity, as well as a linear field range that is orders of magnitude higher than that of xMR sensors. Within the automotive industry, a wide dynamic field range is a requirement for current sensing applications, where currents may be up to 1 kA large, thus generating strong magnetic fields. It is therefore estimated that an applicable magnetic sensor will need a dynamic field range of more than ± 2 kOe [9]. One successful method to increase the field range of TMR sensors is the use of a magnetic vortex structure in the magnetic free layer (FL), which yields linear ranges in the order of 500 Oe [10–13]. In this work, we utilize perpendicular magnetic anisotropy (PMA) in the reference system, while the FL has in-plane anisotropy [14–21]. This cross-geometric anisotropy in xMR sensor technology has realized TMR sensors of up to ± 5.6 kOe dynamic range [15]. Here, we present GMR sensors with perpendicular synthetic antiferromagnets (p-SAF) as reference system of up to

10 kOe exchange coupling field H_{ex} [22, 23], enabling accordingly wide dynamic ranges. We study the impact of the FL saturation field on GMR transfer curves, using superconducting quantum interference device - vibrating sample magnetometry (SQUID-VSM), polar magneto-optic Kerr effect (MOKE), and GMR measurement setups. The high H_{ex} in the reference system and the FL saturation field control are achieved by using Co/Pt multilayer (ML) systems [22, 24–27], where PMA stems from strong spin-orbit coupling and d - d orbital hybridization at the interface [24, 28, 29]. The behavior in magnetization reversal and magnetoresistance are further investigated through micromagnetic simulations, focusing on switching fields and spin-canting effects [30, 31] within the p-SAF reference system.

II. EXPERIMENTAL DETAILS

Films were deposited onto thermally oxidized silicon (100) substrates in a BESTEC magnetron-sputtering chamber with a base pressure of 1×10^{-8} mbar. Argon was used as a sputter gas during the deposition process with a pressure of 5×10^{-3} mbar at room temperature. For this work, two different types of p-SAF reference systems were fabricated, which differ in their number of interlayer exchange coupling spacer layers [32]. For single p-SAF systems, we used the following stack structure: substrate/Ta(50)/Ru(100)/Pt(20)/[Co(3)/Pt(2)]₅/Co(3)/Ru(4)/[Co(3)/Pt(3)]₅/Co(4)/cap (thicknesses in Å). The double p-SAF structures are composed of substrate/Ta(50)/Ru(100)/Pt(20)/[Co(3)/Pt(2)]_X/Co(3)/Ru(4)/[Co(3)/Pt(3)]_Y/Co(3)/Ru(4)/Co(10)/cap, where X and Y refer to the respective number of bilayers in the ML, which

* clemens.muehlenhoff@physik.uni-augsburg.de

† christoph.vogler@univie.ac.at

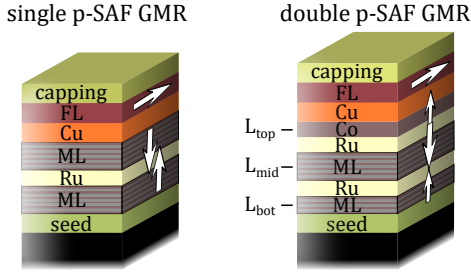


FIG. 1. Illustrations of the employed single and double p-SAF GMR stacks. While the single p-SAF uses only one Ru spacer layer, the double p-SAF incorporates two spacer layers for interlayer exchange coupling. Thus, double p-SAFs consist of three antiferromagnetically coupled ferromagnetic layers, L_{bot} , L_{mid} , and L_{top} . White arrows illustrate magnetization directions at zero field.

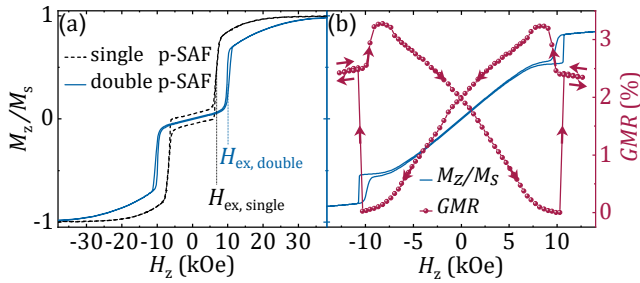


FIG. 2. (a) Comparison of normalized magnetization curves, taken from SQUID-VSM measurements of a single and double p-SAF. (b) Magnetization and GMR signal of a GMR sensor with a double p-SAF reference system, yielding $H_{\text{ex}} = 10$ kOe, and a FL system of type S_b ($t_{\text{Co}} = 20$ Å). Red arrows in the GMR transfer curve represent the direction of the magnetic field sweep.

vary depending on the sample's purpose. P-SAFs reveal the highest exchange fields for $X=4$ and $Y=7$, whereas p-SAFs for the investigation of FL saturation fields and spin-canting effects are built with $X=6$, and $Y=8$. Illustrations of the two types of samples are given in Fig. 1, showing a single and double p-SAF GMR stack with three ferromagnetic layers L_{bot} , L_{mid} , and L_{top} for the double p-SAF. For complete GMR sensor structures, a 20 Å Cu spacer layer, followed by a magnetic FL were deposited on top of L_{top} . Four different FL systems S_x were fabricated:

- S_a : Co(30),
- S_b : $[\text{Co}(t_{\text{Co}})/\text{Pt}(2.5)]_3$,
- S_c : $\text{Co}(30)/\text{Pt}(2.5)/[\text{Co}(3.5)/\text{Pt}(2.5)]_3$, and
- S_d : $\text{Co}(30)/\text{CoFe}(30)$.

As a capping layer, Pt(20)/Ta(50) was used. The out-of-plane magnetization of all samples was measured in a SQUID-VSM magnetometer and a polar MOKE setup at room temperature. Furthermore, GMR measurements were conducted at room temperature in Van-der-Pauw configuration.

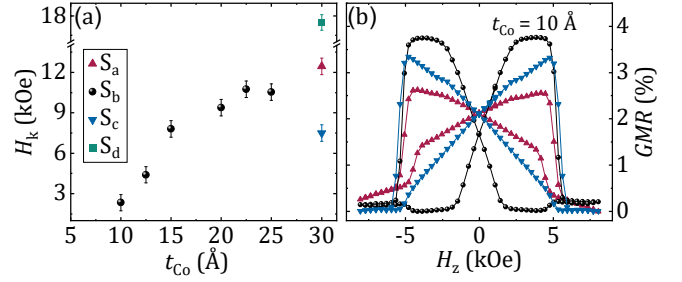


FIG. 3. (a) Free layer H_k values for different FL systems and FL Co layer thicknesses with (b) corresponding GMR transfer curves of single p-SAF GMR sensors.

III. EXPERIMENTAL RESULTS AND DISCUSSION

Figure 2 shows the normalized magnetizations, M_z/M_s , for a single and a double p-SAF in out-of-plane fields, here defined as H_z pointing in z-direction. Even at $H_z < H_{\text{ex}}$ a change in M_z/M_s of 0.9 $\frac{\%}{\text{kOe}}$ is detected for both types of p-SAFs, indicating the occurrence of small spin-canting throughout the field range. Double p-SAF structures yield higher H_{ex} , as in this case $H_{\text{ex}} = 10$ kOe. However, the magnetization still increases at fields above H_{ex} , especially for double p-SAF structures, which again suggests spin-canting of the p-SAF reference system. Systems with H_{ex} of up to 10 kOe are also present in GMR structures using a FL system of type S_b with $t_{\text{Co}} = 20$ Å, as shown in Fig. 2(b). The resistivity R , here represented as the GMR effect with

$$\text{GMR}(\%) = 100 \times \frac{R(H_z) - R_{\text{min}}}{R_{\text{min}}}, \quad (1)$$

shows abrupt changes at the fields of p-SAF layer switching. The FL is designed to magnetically saturate around 9 kOe, which can be seen in the magnetization curves (Fig. 2(b)). However, similarly to Fig. 2(a), the magnetization of the GMR system still increases slightly above H_{ex} . Even more unexpectedly, the resistivity at fields above 10 kOe is still higher than at zero field. This indicates that the p-SAF is not fully saturated and is likely to have its top layer magnetization in a near antiparallel state with that of the saturated FL in order to induce a GMR effect.

In order to exploit the full spectrum of parallel to antiparallel alignment of free and reference layer, the in-plane FL anisotropy needs to be adjusted in such a way that the FL saturates before or at the p-SAF switching field of the reference system. For TMR structures with an MgO barrier and a CoFeB free layer this can be achieved by choosing CoFeB to be appropriately thin so that orbital hybridization at the MgO/CoFeB interface adds perpendicular magnetic anisotropy to the FL system [16, 18]. For our GMR sensors, however, we use four different FL systems to change the FL's magnetic anisotropy. In Fig. 3(a) the effective anisotropy field H_k of each FL system is given, taken from out-of-plane SQUID-VSM measurements including the standard deviation from multiple fabrication

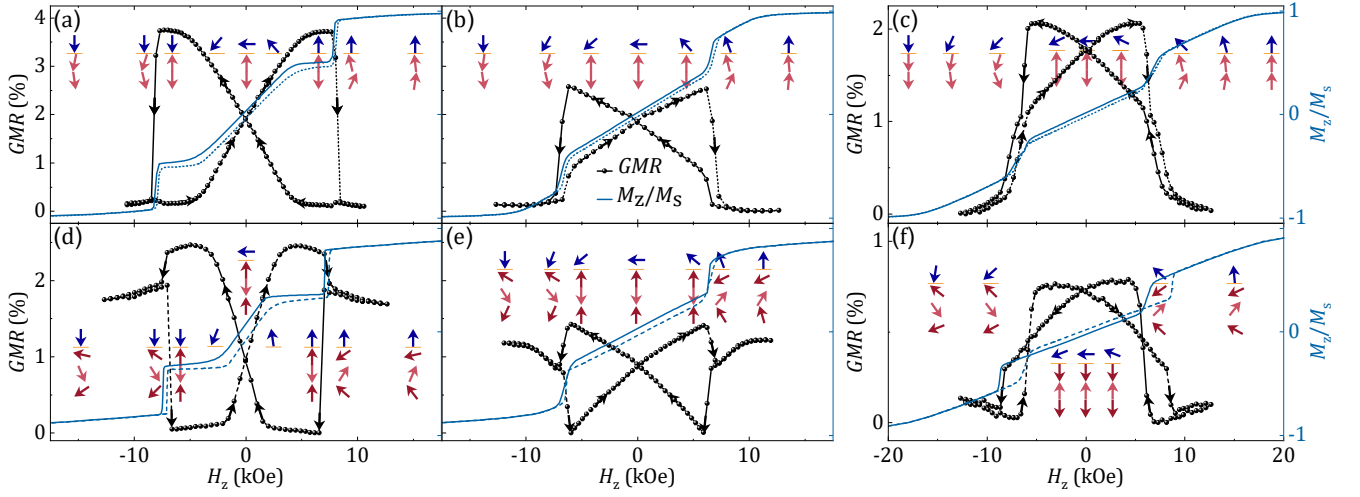


FIG. 4. GMR signals and normalized magnetizations for GMR sensors in out-of-plane fields. GMR sensors with (a-c) single and (d-f) double p-SAF reference system ($X=6$, $Y=8$), and free layer (a,c) $H_k \leq H_{ex}$, (b,e) $H_k > H_{ex}$, and (c,f) $H_k \gg H_{ex}$. The respective FL systems are (a) S_b ($t_{Co}=12.5$ Å), (b) S_b ($t_{Co}=25.0$ Å), (c) S_d , (d) S_b ($t_{Co}=10.0$ Å), (e) S_c , and (f) S_d . The arrows illustrate the possible magnetization directions of the respective layers, with blue representing the free layer and red representing the layers of the p-SAF reference system. Solid lines represent a field sweep from positive to negative saturation, dashes lines from negative to positive saturation.

cycles used as error bars. Figure 3(b) shows examples of corresponding GMR transfer curves. The simplest FL system S_a , represented as red upwards triangles, saturates at 12.5 kOe in H_z . Is the FL designed as a multilayer system of type S_b , the saturation field can be easily adjusted via the specific Co thickness t_{Co} in the ML, here shown as black dots. The effective magnetic anisotropy favors an in-plane easy axis magnetization for $t_{Co} \geq 10$ Å [33, 34], due to the large contribution of magnetic shape anisotropy. For growing t_{Co} the magnetic shape anisotropy increases, leading to a FL saturation at higher out-of-plane fields. Similarly, the FL magnetic saturation field is decreased to approximately 7.5 kOe for a sample with a type S_c FL, where a layer of Co(30) with strong in-plane magnetic anisotropy is coupled to a ML with PMA, here represented with blue downwards triangles. Lastly, adding a CoFe(30) layer to the Co layer in the S_d FL, shown as teal rectangle in Fig. 3(a), significantly increases H_k to 17.5 kOe, which is partly due to the CoFe layer acting as a spacer between the Co free and the Pt capping layer, thus preventing PMA at the Co/Pt interface. The corresponding GMR transfer curves are shown later in Figs. 4(c) and 4(f).

Using the structures mentioned above, we systematically changed H_k of the FL for single and double p-SAF GMR systems, as shown in Fig. 4, with single p-SAFs in Figs. 4(a-c) and double p-SAFs in Figs. 4(d-f). GMR transfer curves as well as normalized $M-H_z$ hysteresis loops from a SQUID-VSM are plotted. The arrows illustrate the assumed magnetization direction of the respective magnetic layers (from positive saturation to negative). Note the different scales for Figs. 4(c) and 4(f). From our measurements, 3 distinct configurations regarding the relation of FL H_k to p-SAF H_{ex} are visible for both single and double p-SAF GMRs in order of appearance in Fig. 4:

(a,d) $H_k \leq H_{ex}$, (b,e) $H_k > H_{ex}$, and (c,f) $H_k \gg H_{ex}$. Generally, the decrease in sensor sensitivity, i.e. the change of GMR over field, with increasing H_k is well visible, as expected. In the following, we discuss the results in more detail, and argue that spin-canting effects offer an explanation for the observed magnetization and GMR transfer curves.

The single p-SAF GMR sensors in Figs. 4(b) and 4(c) show their smallest resistance for $H_z > H_{ex}$, when the FL saturation is reached at H_k . Spin-canting effects in the p-SAF system aren't visible, due to the change of magnetization in the FL. The exception is the sample of Fig. 4(a) with $H_k < H_{ex}$. Here, a small increase in R is visible at H_{ex} , followed by a decrease in R for $H_z > H_{ex}$. This indicates very small spin-canting of the p-SAF reference system for $H_z > H_{ex}$. The double p-SAF GMR sensors in Figs. 4(d-f), on the other hand, show an unexpected high R at $H_z > H_{ex}$. The resistance in Fig. 4(d) gradually decreases for increasing $H_z > H_{ex}$. Since the FL of the sample saturates already before H_{ex} , this decrease is caused by a spin-canted state of the p-SAF reference system and its gradual magnetic alignment with the FL magnetization at higher fields. In Fig. 4(e), the resistance further increases for increasing $H_z > H_{ex}$, until the FL saturation magnetization is reached. A different GMR behavior can be seen in Fig. 4(f), where $H_k \gg H_{ex}$. Here, R is smaller for $H_z > H_{ex}$, indicating a more parallel configuration of FL and reference layer magnetization direction than for $H_z < H_{ex}$. However, with further increasing $H_z > H_{ex}$, magnetization directions rotate to an increasingly antiparallel alignment, owed to the strong spin-canting of the p-SAF reference system. This leads to an increase in R for high fields, in contrast to the decrease that is observed in the case of the same FL but with a single p-SAF reference system, as shown in Fig. 4(c).

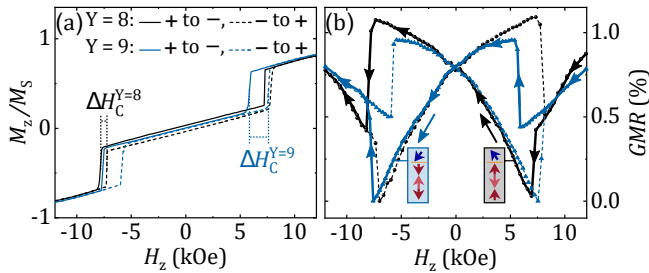


FIG. 5. (a) SQUID-VSM and (b) GMR measurements of double p-SAF GMR sensors with differing bilayer number $Y=8$ (black) and $Y=9$ (blue) in L_{mid} . Positive to negative field sweeps are drawn in solid lines with arrows to guide the eye, negative to positive field sweeps are drawn in dashed lines.

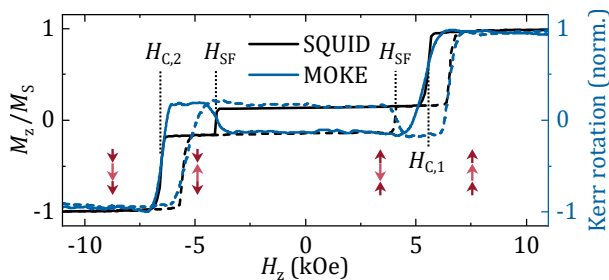


FIG. 6. SQUID-VSM and MOKE measurement of an imbalanced p-SAF with occurring spin flip field H_{SF} .

Summarized, we observe only a small spin-canting behavior for single p-SAF GMR sensors, but strong spin-canting for double p-SAF GMR samples at fields above H_{ex} , which yields significantly different GMR transfer curves.

Depending on the magnetic moments within the double p-SAF structures, either L_{mid} or the outer layers, L_{bot} and L_{top} , switch first. The difference is shown in Fig. 5, where two consecutively fabricated double p-SAF GMR sensors yield a different switching behavior due to a change of M_{StML} in L_{mid} by design, with t_{ML} being the total film thickness of the ML. This increase of M_{StML} is achieved by using a higher number of Co/Pt bilayers $Y=9$ instead of $Y=8$ [26].

IV. MICROMAGNETIC SIMULATION

To understand the experimentally obtained magnetization reversal processes and the corresponding GMR of Fig. 4, the finite-element software package magnum.fe [35] was used to simulate the field dependence of the magnetization of the introduced GMR sensors by means of a spin-chain model. This model consists of a 3D nanorod with a square basal plane of side length $a = 10 \text{ \AA}$, but with a lateral discretization length much larger than 10 \AA . This produces a mesh with nodes only along the edges in lateral direction. Along the easy-axis direction (z direction) a fine mesh with a dis-

In Fig. 5(a) it is visible that the total magnetization reversal and the underlying magnetization profile is similar for both samples, however, with the difference of the $Y=9$ samples showing a significantly higher hysteresis width ΔH_C , which we define by the field difference of p-SAF switching fields $H_{C,1}$ and $H_{C,2}$. A further difference emerges in the comparison of GMR transfer curves in Fig. 5(b). As measurements from positive to negative fields are drawn in solid lines, whereas negative to positive field sweeps are drawn in dashed lines, the transfer curves of the two samples reveal quite different switching behaviors. In a sweep from positive to negative fields, the $Y=8$ sample of lower L_{mid} magnetization jumps from a spin-canted state into a configuration of low GMR, with L_{top} and L_{bot} dominating the p-SAF, pointing parallel to the external magnetic field, and L_{mid} pointing antiparallel (see illustration of magnetization in the right inset). Towards smaller and eventually negative fields, the GMR increases as the FL magnetization rotates into an antiparallel alignment with L_{top} . For the $Y=9$ sample the opposite p-SAF behavior occurs, with L_{mid} dominating the p-SAF, leading to a decrease of GMR with decreasing fields, as illustrated in the left inset. Since our samples in Fig. 4 were designed with balanced magnetic moments of the respective magnetic layers, even small fluctuations during the fabrication process may lead to a different switching behavior. This is demonstrated in the GMR sensor plotted in Fig. 4(f) in contrast to those plotted in 4(d) and 4(e). It has to be noted that in case of highly imbalanced p-SAF structures, an additional switching can occur [22], as presented in Fig. 6. Here, SQUID-VSM and MOKE measurements show a spin flip of the p-SAF at H_{SF} between the switching fields $H_{C,1}$ and $H_{C,2}$, where the coupled p-SAF system reverses its magnetization orientations, keeping the preferred antiparallel alignment. This results in a smaller net magnetization detected by SQUID-VSM but an increased Kerr rotation detected by MOKE, which is more sensitive towards magnetization changes of the top layers. Note, that in this case, the possible linear range of a GMR sensor is limited by H_{SF} instead of $H_{C,1}$.

In order to confirm our findings and to unravel the underlying reversal processes, micromagnetic simulations were carried out.

cretization length of approximately 5 \AA is used. The reference material parameters for the layers of both investigated p-SAFs are based on the experimental data and are summarized in Table I.

In the micromagnetic simulations single ferromagnetic layers with the properties of the p-SAF multilayers are computed. The modeling is started with a positive external saturation field of 30 kOe with all layers pointing in the $+z$ direction. The field is applied with an angle of 5° with respect to the easy axis to avoid metastable states. Then, the magnetic field magnitude is decreased stepwise in -0.5 kOe increments to -30 kOe and back to $+30 \text{ kOe}$. After each field-step the micromagnetic state of the system is relaxed for

	single p-SAF		double p-SAF		
	L_{bot}	L_{top}	L_{bot}	L_{mid}	L_{top}
K_{eff} (Merg/cm ³)	3.49	3.99	2.99 ^{7e} /4.49 ^{7d,7f}	3.99 ^{7e} /4.49 ^{7d,7f}	-0.01
M_S (kemu/cm ³)	1.15	1.35	1.43	<u>1.15</u> ^{7d,7e} /1.31 ^{7f}	<u>1.75</u> ^{7d,7e} /1.67 ^{7f}
A_{ex} (μ erg/cm)	1.0	1.0	1.0	1.0	1.0
J_{ex} (erg/cm ²)		-2.5		-2.5	-2.5
α	1.0	1.0	1.0	1.0	1.0
a (\AA)	10	10	10	10	10
t (\AA)	28	29	33	45	10

TABLE I. Material parameters of the simulated single p-SAF and double p-SAF systems for all involved layers. K_{eff} is the effective uniaxial magnetic anisotropy constant, M_S is the saturation magnetization, A_{ex} is the bulk exchange constant within the layers, J_{ex} is the interface exchange coupling between the layers, α is the dimensionless damping constant, a is the lateral side length of the simulated nanorod and t is the thickness of the layers. The superscript symbols in the values of K_{eff} and M_S refer to the used parameters in the subplots of Fig. 7. The underlined parameters indicate the basis parameters that are used unless otherwise specified.

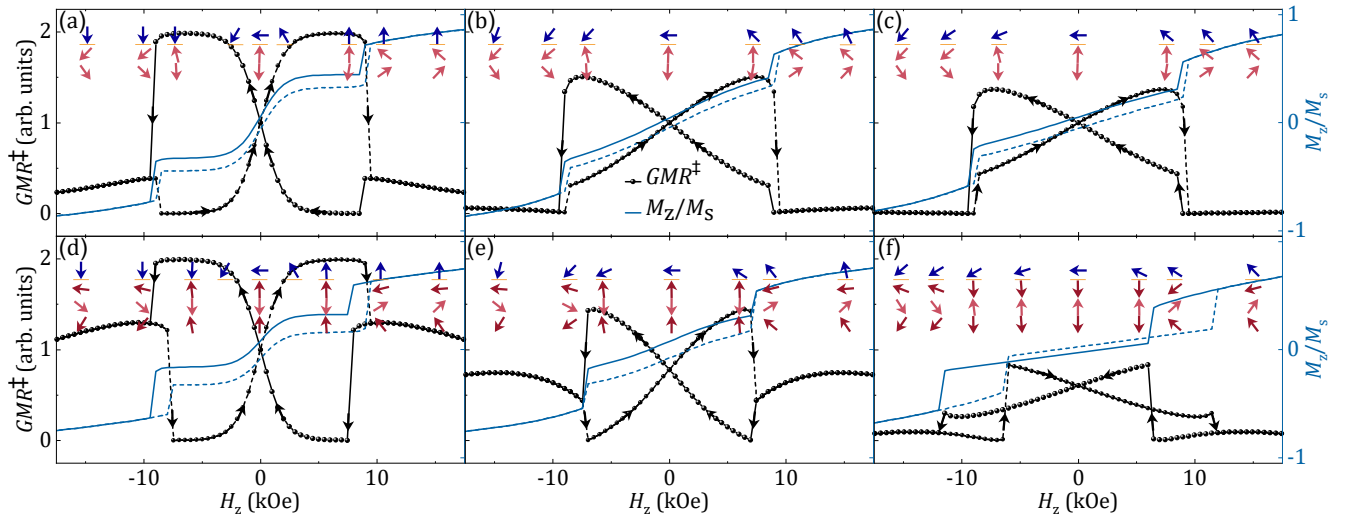


FIG. 7. Simulation results for GMR^+ signals and normalized magnetizations for GMR sensors in out-of-plane fields. GMR sensors with (a-c) single and (d-f) double p-SAF reference system, and free layer (a,c) $H_k \leq H_{\text{ex}}$, (b,e) $H_k > H_{\text{ex}}$, and (c,f) $H_k \gg H_{\text{ex}}$. The arrows illustrate simulated magnetization directions of the respective layers, with blue representing the free layer and red representing the layers of the p-SAF reference system.

100 ns. Note, that the variation of the applied field in the modeling work is performed much faster than that used during the acquisition of the measurement data. However, because a high damping constant ($\alpha = 1.0$) is used in the modeling work, a stationary state is obtained within 100 ns, such that the modeled loops are representative for the experimental loops.

To qualitatively model the GMR [36] from the simulated hysteresis loops, we use the enclosed magnetization angle γ of the free layer and the top p-SAF layer per:

$$GMR^{\pm} = 1 - \cos(\gamma). \quad (2)$$

Note, that for simplicity the free layer magnetization is not simulated. Instead it is modeled with a generic tanh function, where the thickness, the saturation field and the saturation magnetization of the free layer are

chosen according to the measured sensor stacks (see Fig. 4).

With the spin-chain model and the material parameters of Tab. I we obtain an excellent qualitative agreement with the measurements in both the magnetization data as well as in the GMR, as illustrated in Fig. 7. The spin-canting of the p-SAF layers obtained from the simulations also agrees well with that extracted from the GMR measurements of Fig. 4. Note, that our simulations also show a small spin-canting of the p-SAF at small fields as hypothesized earlier from Fig. 2(a). To achieve this agreement, some, at this point, seemingly arbitrary variations were made to the material parameters of the individual layers of the double p-SAF system. The parameter variations are given by the superscripts, containing the corresponding reference figure to which they refer, in Tab. I.

In the following we will make a more systematic anal-

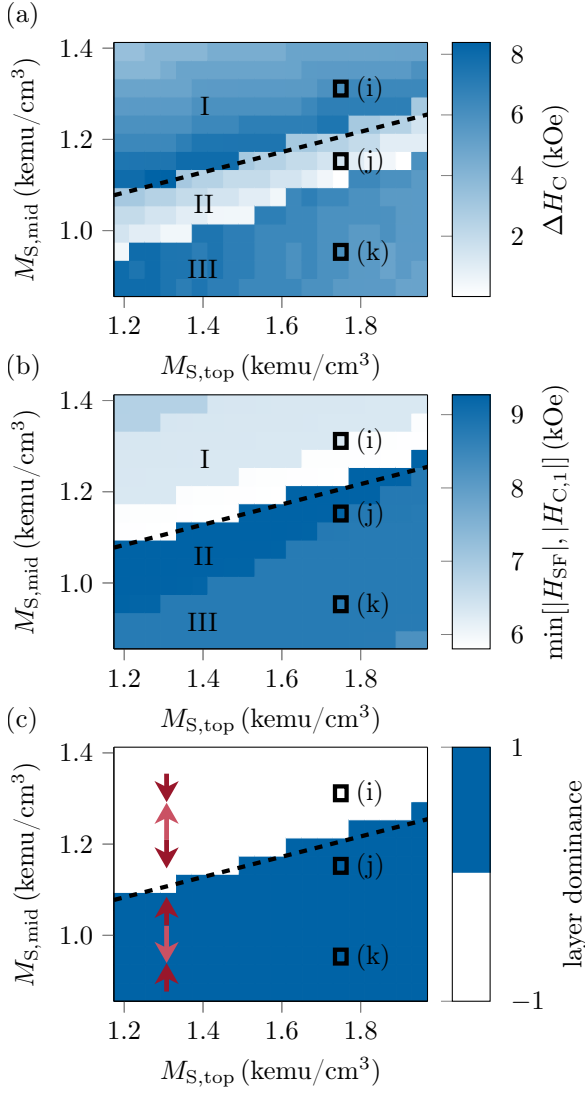


FIG. 8. Characteristic properties of the hysteresis loops of the double p-SAF system for variations of the saturation magnetizations of the top and the middle p-SAF layer. All material parameters that are not varied are taken from Tab. I. The properties are (a) the hysteresis loop width ΔH_C , (b) the linear range of the sensor stack defined as $\min[|H_{SF}|, |H_{C,1}|]$ and (c) the layer dominance with respect to the external field. The arrows illustrate the meaning of the dominance by showing the reversal mechanism of the layers for a decreasing external field coming from positive saturation. The dashed line illustrates the border between the regions of dominance.

ysis of the influences of the most important parameters for the double p-SAF structures. Based on the reference parameters of Tab. I (underlined values if more than one is given) we start with the saturation magnetization of the layers and vary that of L_{top} in the range of 1.19 kemu/cm³ to 1.95 kemu/cm³ and that of L_{mid} in the range of 0.88 kemu/cm³ to 1.39 kemu/cm³, while keeping the properties of L_{bot} constant. In both cases a step size of $\Delta M_S = 0.02$ kemu/cm³ is used. Figure 8 displays three interesting properties of the resulting hysteresis loops, namely the hysteresis width ΔH_C , the linear range, which is defined as $\min[|H_{C,1}|, |H_{SF}|]$

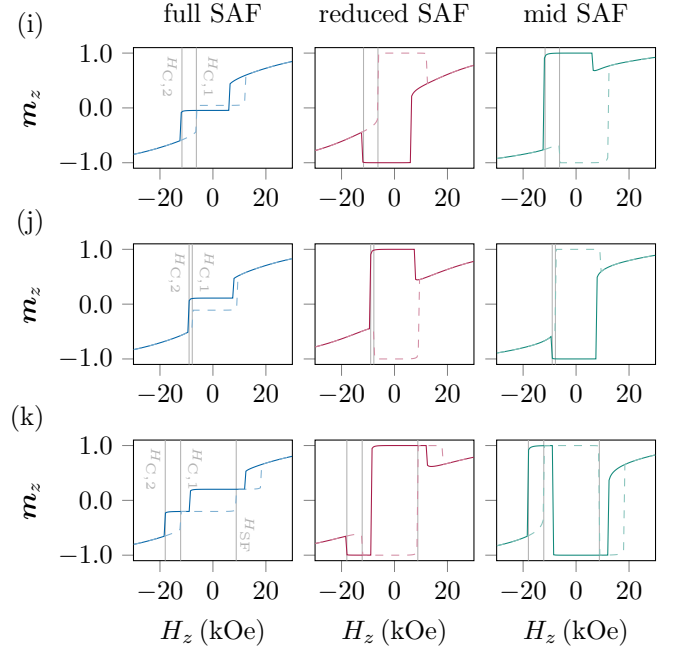


FIG. 9. Normalized z component of the magnetization of the full double p-SAF system, the middle p-SAF layer and a reduced p-SAF layer as introduced in Eq. 3. The magnetization for decreasing fields coming from positive saturation is illustrated with a solid line and that of for increasing saturation fields coming from negative saturation is shown with a dashed line. (i), (j) and (k) refer to the phase points marked in Fig. 8. The vertical lines indicate the switching fields $H_{C,1}$ and $H_{C,2}$ and the spin-flip field H_{SF} (introduced in Fig. 6).

(see Fig. 6), and the layer dominance of the p-SAF with respect to the external field. As shown in the inset of Fig. 8(c), a value of -1 means that, when coming from saturation, the top layer switches into an antiparallel direction with respect to the external magnetic field, while a value of $+1$ means that the middle layer switches, which leaves the top layer magnetization direction and external field in a parallel configuration. Obviously, the two regions show either the middle p-SAF layer or the outer two ones being aligned with the external field. In contrast to Figs. 8(b) and (c) three regions appear (labeled with I, II and III) in the minor loop hysteresis width of Fig. 8(a). While the border between regions I and II is identical to that of Fig. 8(c), it is not a priori clear why there is an additional border between regions II and III.

To gain deeper insights into the magnetization dynamics, we investigate three phase points of Fig. 8 in more detail. Figure 9 illustrates the hysteresis loops of phase points (i), (j) and (k). In detail, the normalized magnetization of the full double p-SAF is shown in the first column and that of L_{mid} is shown in the last column. To lower the complexity of the system L_{top} and L_{bot} are reduced to a single layer with the following

properties:

$$K_{\text{eff,red}} = \frac{K_{\text{eff,top}}t_{\text{top}} + K_{\text{eff,bot}}t_{\text{bot}}}{t_{\text{top}} + t_{\text{bot}}}$$

$$M_{\text{S,red}} = \frac{M_{\text{S,top}}t_{\text{top}} + M_{\text{S,bot}}t_{\text{bot}}}{t_{\text{top}} + t_{\text{bot}}} \quad (3)$$

This reduction implicitly assumes a parallel alignment of L_{top} and L_{bot} , which is not strictly true at least during the reversal. But this simplified picture is much more instructive and most importantly it is sufficient to characterize the magnetization dynamics correctly. In the middle column of Fig. 9 the dynamics of this reduced layer is displayed. Additionally, the magnetizations for decreasing fields from positive to negative saturation are displayed with solid lines, while the magnetizations for increasing fields from negative to positive saturation are displayed with dashed lines.

A typical hysteresis loop for region I in Fig. 8 with high $M_{\text{S,mid}}$ and low $M_{\text{S,top}}$, and thus low $M_{\text{S,red}}$ is shown in Fig. 9(i). In agreement with Fig. 8(c), we see that L_{mid} dominates the magnetization process. Hence, the switching field of L_{mid} determines the outer part of the hysteresis loop (vertical line with label $H_{\text{C},2}$ in Fig. 9) and the field at which the reduced p-SAF layer switches back to an antiparallel state determines the inner part of the hysteresis loop (vertical line with label $H_{\text{C},1}$ in Fig. 9). We will call the latter field back-switching field. Since the switching fields are inversely proportional to the saturation magnetization, we see an increase of $H_{\text{C},1}$ towards lower values of $M_{\text{S,top}}$ for fixed $M_{\text{S,mid}}$ in Fig. 8(a). This results in an increasing linear range and a decrease of ΔH_{C} . If $M_{\text{S,mid}}$ decreases from 1.31 kemu/cm³ to 1.11 kemu/cm³ and the saturation magnetization of the reduced layer remains fixed, we arrive at phase point (j) and the hysteresis loops of Fig. 9(j). Here, the reduced p-SAF layer is dominating the reversal. Since it has a higher magnetic moment its switching field $H_{\text{C},2}$ is much lower than that of L_{mid} in region I. It is slightly higher than the backswitching field $H_{\text{C},1}$ of L_{mid} resulting in a very small ΔH_{C} . Due to the change of dominance $H_{\text{C},1}$ is now determined by L_{mid} . Hence, the linear range in region II is significantly higher than that in region I. The effect of the decrease of $M_{\text{S,mid}}$ from region I to region II can also be clearly seen in the SQUID-VSM measurements of Fig. 5, where the decrease is caused by changing the layer numbers in L_{mid} . Within region II the linear range further increases with decreasing $M_{\text{S,mid}}$. In contrast, ΔH_{C} decreases with decreasing $M_{\text{S,mid}}$, since $H_{\text{C},1}$ comes closer to $H_{\text{C},2}$. Note, due to the antiferromagnetic exchange coupling, the magnitude of the switching field from an antiparallel to a parallel state is higher than that back to the antiparallel state. The experimental hysteresis loops for different layer numbers in L_{mid} shown in Fig. 5 agree very well with the spin-chain simulations, and thus confirm the influence of an increasing magnetic moment of the middle p-SAF layer in region II.

For even lower $M_{\text{S,mid}}$ we see an abrupt increase of ΔH_{C} in Fig. 8(a). The reason is illustrated in Fig. 9(k). At the switching field of the dominating reduced p-SAF

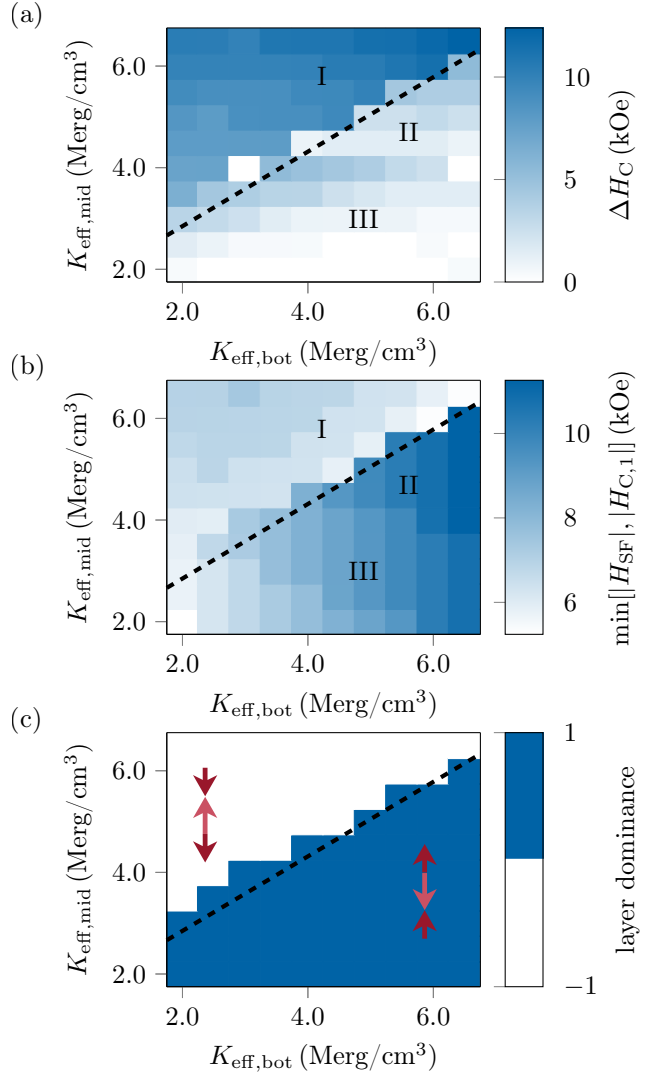


FIG. 10. Characteristic properties of the hysteresis loops of the double p-SAF system for variations of the effective uniaxial magnetic anisotropy of the top and the middle p-SAF layer. All material parameters that are not varied are taken from Tab. I. The properties are (a) the hysteresis loop width ΔH_{C} , (b) the linear range of the sensor stack defined as $\min[|H_{\text{SF}}|, |H_{\text{C},1}|]$ and (c) the layer dominance with respect to the external field. The arrows illustrate the meaning of dominance by showing the reversal mechanism of the layers for a decreasing external field coming from positive saturation. The dashed line illustrates the border between the regions of dominance.

layer a spin flip occurs. The reason is that the switching field of L_{mid} is much larger than that of the reduced layer. Therefore the reduced layer becomes dominant after the spin flip and determines both the switching field $H_{\text{C},2}$ and the backswitching field $H_{\text{C},1}$. This switching behavior can also clearly be seen in Fig. 6.

But not only the saturation magnetization has an influence on the hysteresis of the double p-SAF. However, since a systematic analysis of all possible influences goes beyond the scope of this work, we will exemplarily discuss the variation of the effective magnetic anisotropies of the bottom and the middle layer with constant $K_{\text{eff,top}} = -0.01$ Merg/cm³ in the following.

Figure 10 displays the hysteresis loop width, the linear range and the layer dominance for K_{eff} of both layers in the range of 1.99 Merg/cm³ to 6.49 Merg/cm³ with $\Delta K_{\text{eff}} = 0.5$ Merg/cm³. We again see three regions that represent the same types of hysteresis loops as those in Fig. 8. In region I, L_{mid} dominates the reversal process under an applied magnetic field, while in regions II and III the reduced p-SAF layer dominates. Region II again shows spin-flip processes. Figure 10 again proves that the magnetic anisotropy is as important as the saturation magnetization of the individual layers if we want to describe the reversal mechanism of the double p-SAF.

V. CONCLUSION

In conclusion, we have developed p-SAFs with up to 10 kOe exchange fields based on Co/Pt multilayers, using both single and double structures for interlayer exchange coupling. These p-SAFs were implemented in GMR sensors with perpendicular reference layer and in-plane free layer, yielding up to 8 kOe dynamic field range. We designed different free layer systems, further utilizing Co/Pt multilayers, which yield varied magnetic anisotropies in out-of-plane fields. In

combination with our p-SAF structures, the magnetic anisotropy variation revealed spin-canting effects in the interlayer exchange coupled reference system, predominantly in the double p-SAF GMR sensors. Micro-magnetic simulations based on finite-element spin-chain models further investigated spin-canting effects and p-SAF switching behavior in respect to individual layer saturation magnetization and magnetic anisotropy. Experimental data and simulation results highly agree with one another. The results provide a better understanding of magnetoresistive sensor design and design potentials. However, while double p-SAFs offer a very large design flexibility, one needs to be very careful that uncontrollable variations in the material properties due to the growth of the structure, do not lead to undesired effects.

VI. ACKNOWLEDGMENTS

This study has been supported by the Austrian Science Fund under Grant I2214-N20, and is gratefully acknowledged. The support of the CD-Labor AMSEN (financed by the Federal Ministry of Economics, Family and Youth, the National Foundation for Research, Technology and Development) is acknowledged.

-
- [1] W. Butler, X.-G. Zhang, D. Nicholson, and J. MacLaren, Spin-dependent scattering and giant magnetoresistance, *Journal of Magnetism and Magnetic Materials* **151**, 354 (1995).
 - [2] X. Zhang and W. Butler, *Handbook of Spintronics*, edited by Y. Xu, D. D. Awschalom, and J. Nitta (Springer Netherlands, Dordrecht, 2014) pp. 1–56, ISBN: 978-94-007-7604-3.
 - [3] A. Hirohata and K. Takanashi, Future perspectives for spintronic devices, *Journal of Physics D: Applied Physics* **47**, 193001 (2014).
 - [4] A. Hirohata, H. Sukegawa, H. Yanagihara, I. Zutic, T. Seki, S. Mizukami, and R. Swaminathan, Roadmap for emerging materials for spintronic device applications, *IEEE Transactions on Magnetics* **51**, 1 (2015).
 - [5] C. Zheng, K. Zhu, S. Cardoso de Freitas, J. Chang, J. E. Davies, P. Eames, P. P. Freitas, O. Kazakova, C. Kim, C. Leung, S. Liou, A. Ognev, S. N. Piramanayagam, P. Ripka, A. Samardak, K. Shin, S. Tong, M. Tung, S. X. Wang, S. Xue, X. Yin, and P. W. T. Pong, Magnetoresistive sensor development roadmap (non-recording applications), *IEEE Transactions on Magnetics* **55**, 1 (2019).
 - [6] E. Y. Tsymlal and I. Zutic, eds., *Handbook of Spin Transport and Magnetism* (Chapman and Hall/CRC, 2012) pp. 665–730, ISBN: 978-1-4398-0378-3.
 - [7] S. Ikeda, J. Hayakawa, Y. Ashizawa, Y. M. Lee, K. Miura, H. Hasegawa, M. Tsunoda, F. Matsukura, and H. Ohno, Tunnel magnetoresistance of 604% at 300K by suppression of Ta diffusion in CoFeB $\bar{\text{A}}\bar{\text{L}}\bar{\text{T}}\bar{\text{M}}$ -gO $\bar{\text{A}}\bar{\text{L}}\bar{\text{T}}$ CoFeB pseudo-spin-valves annealed at high temperature, *Applied Physics Letters* **93**, 082508 (2008).
 - [8] G. Binasch, P. Grünberg, F. Saurenbach, and W. Zinn, Enhanced magnetoresistance in layered magnetic structures with antiferromagnetic interlayer exchange, *Physical Review B* **39**, 4828 (1989).
 - [9] T. Ogasawara, M. Oogane, M. Tsunoda, and Y. Ando, Large exchange coupling field in perpendicular synthetic antiferromagnetic structures with CoPt alloy, *Japanese Journal of Applied Physics* **57**, 088004 (2018).
 - [10] D. Suess, A. Bachleitner-Hofmann, A. Satz, H. Weitensfelder, C. Vogler, F. Bruckner, C. Abert, K. Prügl, J. Zimmer, C. Huber, S. Luber, W. Raberg, T. Schrefl, and H. Brückl, Topologically protected vortex structures for low-noise magnetic sensors with high linear range, *Nature Electronics* **1**, 362 (2018).
 - [11] H. Weitensfelder, H. Brueckl, A. Satz, K. Pruegl, J. Zimmer, S. Luber, W. Raberg, C. Abert, F. Bruckner, A. Bachleitner-Hofmann, R. Windl, and D. Suess, Comparison of sensitivity and low-frequency noise contributions in giant-magnetoresistive and tunneling-magnetoresistive spin-valve sensors with a vortex-state free layer, *Phys. Rev. Applied* **10**, 054056 (2018).
 - [12] T. Wurft, W. Raberg, K. Prügl, A. Satz, G. Reiss, and H. Brückl, The influence of edge inhomogeneities on vortex hysteresis curves in magnetic tunnel junctions, *IEEE Transactions on Magnetics* **53**, 1 (2017).
 - [13] T. Wurft, W. Raberg, K. Prügl, A. Satz, G. Reiss, and H. Brückl, Evolution of magnetic vortex formation in micron-sized disks, *Applied Physics Letters* **115**, 132407 (2019).
 - [14] F. B. Mancoff, J. Hunter Dunn, B. M. Clemens, and R. L. White, A giant magnetoresistance sensor for high magnetic field measurements, *Applied Physics Letters* **77**, 1879 (2000).
 - [15] T. Ogasawara, M. Oogane, M. Al-Mahdawi, M. Tsunoda, and Y. Ando, Effect of second-order magnetic anisotropy on nonlinearity of conductance in CoFeB/MgO/CoFeB magnetic tunnel junction for magnetic sensor devices, *Scientific Reports* **9**, 17018 (2019).

- [16] T. Nakano, M. Oogane, T. Furuichi, and Y. Ando, Magnetic tunnel junctions using perpendicularly magnetized synthetic antiferromagnetic reference layer for wide-dynamic-range magnetic sensors, *Applied Physics Letters* **110**, 012401 (2017).
- [17] H. X. Wei, Q. H. Qin, Z. C. Wen, X. F. Han, and X.-G. Zhang, Magnetic tunnel junction sensor with Co/Pt perpendicular anisotropy ferromagnetic layer, *Applied Physics Letters* **94**, 172902 (2009).
- [18] P. Wisniewski, J. Wrona, T. Stobiecki, S. Cardoso, and P. P. Freitas, Magnetic Tunnel Junctions Based on Out-of-Plane Anisotropy Free and In-Plane Pinned Layer Structures for Magnetic Field Sensors, *IEEE Transactions on Magnetics* **48**, 3840 (2012).
- [19] P. Matthes and M. Albrecht, Pseudo spin valve thin films with crossed magnetic anisotropies, *Sensors and Actuators A: Physical* **233**, 275 (2015).
- [20] P. Matthes, S. S. P. K. Arekapudi, F. Timmermann, and M. Albrecht, Magnetotransport properties of perpendicular [pt/co]/cu/[co/pt] pseudo-spin-valves, *IEEE Transactions on Magnetics* **51**, 1 (2015).
- [21] T. Nakano, M. Oogane, T. Furuichi, and Y. Ando, Magnetic-sensor performance evaluated from magneto-conductance curve in magnetic tunnel junctions using in-plane or perpendicularly magnetized synthetic antiferromagnetic reference layers, *AIP Advances* **8**, 045011 (2018).
- [22] K. Yakushiji, H. Kubota, A. Fukushima, and S. Yuasa, Perpendicular magnetic tunnel junctions with strong antiferromagnetic interlayer exchange coupling at first oscillation peak, *Applied Physics Express* **8**, 083003 (2015).
- [23] K. Yakushiji, A. Sugihara, A. Fukushima, H. Kubota, and S. Yuasa, Very strong antiferromagnetic interlayer exchange coupling with iridium spacer layer for perpendicular magnetic tunnel junctions, *Applied Physics Letters* **110**, 092406 (2017).
- [24] M. T. Johnson, P. J. H. Bloemen, F. J. A. den Broeder, and J. J. de Vries, Magnetic anisotropy in metallic multilayers, *Reports on Progress in Physics* **59**, 1409 (1996).
- [25] J. Chatterjee, T. Tahmasebi, S. Mertens, G. S. Kar, T. Min, and J. D. Boeck, Seed layer effect on the magnetic properties of ultrathin co/pt multilayers with perpendicular magnetic anisotropy, *IEEE Transactions on Magnetics* **50**, 1 (2014).
- [26] K. Yakushiji, T. Saruya, H. Kubota, A. Fukushima, T. Nagahama, S. Yuasa, and K. Ando, Ultrathin co/pt and co/pd superlattice films for mgo-based perpendicular magnetic tunnel junctions, *Applied Physics Letters* **97**, 232508 (2010).
- [27] J. Chatterjee, S. Auffret, R. Sousa, P. Coelho, I.-L. Prejbeanu, and B. Dieny, Novel multifunctional rky coupling layer for ultrathin perpendicular synthetic antiferromagnet, *Scientific Reports* **8**, 11724 (2018).
- [28] M. T. Johnson, R. Jungblut, P. J. Kelly, and F. J. A. Den Breder, Perpendicular magnetic anisotropy of multilayers: recent insights, *Journal of Magnetism and Magnetic Materials* **148**, 118 (1995).
- [29] N. Nakajima, T. Koide, T. Shidara, H. Miyauchi, H. Fukutani, A. Fujimori, K. Iio, T. Katayama, M. Nývlt, and Y. Suzuki, Perpendicular Magnetic Anisotropy Caused by Interfacial Hybridization via Enhanced Orbital Moment in Co/Pt Multilayers: Magnetic Circular X-Ray Dichroism Study, *Physical Review Letters* **81**, 5229 (1998).
- [30] M. S. Ackermann and S. Emori, Switching of biaxial synthetic antiferromagnets: A micromagnetic study, *Journal of Applied Physics* **124**, 223901 (2018).
- [31] A. Fernández-Pacheco, E. Vedmedenko, F. Ummelen, R. Mansell, D. Petit, and R. P. Cowburn, Symmetry-breaking interlayer Dzyaloshinskii-Moriya interactions in synthetic antiferromagnets, *Nature Materials* **18**, 679 (2019).
- [32] P. Bruno, Theory of interlayer magnetic coupling, *Physical Review B* **52**, 411 (1995).
- [33] F. den Broeder, W. Hoving, and P. Bloemen, Magnetic anisotropy of multilayers, *Journal of Magnetism and Magnetic Materials* **93**, 562 (1991).
- [34] K. Yakushiji, H. Kubota, A. Fukushima, and S. Yuasa, Perpendicular magnetic tunnel junction with enhanced anisotropy obtained by utilizing an ir/co interface, *Applied Physics Express* **9**, 013003 (2015).
- [35] C. Abert, L. Exl, F. Bruckner, A. Drews, and D. Suess, magnum.fe: A micromagnetic finite-element simulation code based on FEniCS, *Journal of Magnetism and Magnetic Materials* **345**, 29 (2013).
- [36] B. Dieny, V. S. Speriosu, S. S. P. Parkin, B. A. Gurney, D. R. Wilhoit, and D. Mauri, Giant magnetoresistive in soft ferromagnetic multilayers, *Physical Review B* **43**, 1297 (1991).